Low-energy photoelectron imaging spectroscopy of nitromethane anions: Electron affinity, vibrational features, anisotropies, and the dipole-bound state

Christopher L. Adams, Holger Schneider, Kent M. Ervin, and J. Mathias Weber

Citation: The Journal of Chemical Physics **130**, 074307 (2009); doi: 10.1063/1.3076892
View online: https://doi.org/10.1063/1.3076892
View Table of Contents: http://aip.scitation.org/toc/jcp/130/7
Published by the American Institute of Physics

Low-energy photoelectron imaging spectroscopy of nitromethane anions: Electron affinity, vibrational features, anisotropies, and the dipole-bound state

Christopher L. Adams, Holger Schneider, Kent M. Ervin,[a] and J. Mathias Weber[b]
JILA, NIST, and Department of Chemistry and Biochemistry, University of Colorado, Boulder, Colorado 80309, USA

(Received 1 October 2008; accepted 9 January 2009; published online 20 February 2009)

We present low-energy velocity map photoelectron imaging results for nitromethane anions. The photoelectron spectrum is interpreted with the aid of *ab initio* theory and Franck–Condon factor calculations. We obtain a new value for the adiabatic electron affinity of nitromethane of (172 ± 6) meV and observe the dipole-bound state of nitromethane. The photoelectron angular distributions of the observed features are discussed in the context of threshold laws for photodetachment. © *2009 American Institute of Physics*. [DOI: 10.1063/1.3076892]

I. INTRODUCTION

The interaction of nitromethane (CH_3NO_2) with low-energy electrons and the properties of the $CH_3NO_2^-$ anion have been the subject of many studies, both experimentally[1–5] and theoretically.[6,7] One very remarkable feature of CH_3NO_2 is that it has a sufficiently high dipole moment [$\mu = 3.46$ D (Ref. 1)] to bind an excess electron not only in a valencelike state but also in a state that is more accurately described as a dipole-bound state.[1,2,6,8] The binding energy of the valencelike state is comparatively small,[1] below several of the fundamental vibrational transitions in the anion, making it an ideal model system for the investigation of the interaction of vibrational excitation and electron emission.[3,5] Interestingly, the signature of the dipole-bound state of $CH_3NO_2^-$ has not been found in photoelectron (PE) spectroscopy so far.[1]

The adiabatic electron affinity (AEA) of CH_3NO_2 has been determined to be (260 ± 80) meV by Compton *et al.*[1] by using the last discernible peaks on a very extended and congested vibrational progression as bracketing features. The error bars were intended to cover the range of possible origin assignments of a vibrational progression with (80 ± 9) meV (645 cm^{-1}) spacing, yielding possible EAs of about 180, 260, or 340 meV. In light of the interest in the interaction of CH_3NO_2 with low-energy electrons and investigations of vibration-electron interaction, a more accurate determination of the AEA is desirable. This can be achieved using near-threshold PE imaging spectroscopy. Pioneered by Osterwalder *et al.*,[9] this method yields extremely high resolution in the limit of low PE kinetic energies.

The extended and congested vibrational progressions that made earlier AEA measurements difficult is based on the large differences in the geometry of the nitro group between the anion and the neutral molecule. In the neutral molecule, the CN bond lies in the ONO plane, while the nitro group is strongly angled away from the CN bond in the anion geometry (see Fig. 1). The vibrational spacing found in the PE spectrum reported by Compton *et al.*[1] is consistent with both the NO_2 bending mode and the NO_2 wagging mode of the neutral molecule. In this paper, we present low-energy PE imaging results for the $CH_3NO_2^-$ anion, revealing much more detail. At the same time, CH_3NO_2 is small enough to be tractable by *ab initio* theory, facilitating a deeper interpretation of the PE spectrum through calculations of Franck–Condon factors (FCFs).

Anions from typical supersonic expansion sources can have high temperatures, often several hundred K. Ar solvation of the target ions can be used to cool them to much lower temperatures, since the binding energies of Ar atoms to anions are low (on the order of a few hundred cm^{-1}).[3] As the vibrational modes of the neutral molecule will usually not be strongly affected by the presence of an Ar atom, Ar solvation is a convenient way to suppress hot bands, while still maintaining the general pattern of the PE spectrum, shifted by the Ar solvation energy of the anion.[10] We are able to unambiguously determine the feature corresponding to the vibrational ground state in the PE spectrum by comparing the PE spectrum of bare (and relatively warm) $CH_3NO_2^-$ with that of cold $CH_3NO_2^- \cdot Ar$, and arrive at a new value for the AEA of CH_3NO_2 of (172 ± 6) meV. We tentatively assign a weak signature in the PE spectrum to the dipole-bound state. Finally, we discuss the angular distributions of the observed

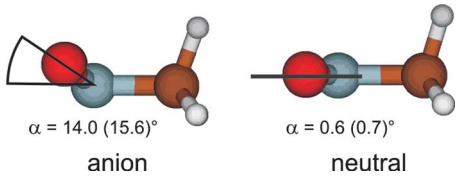

FIG. 1. (Color online) Geometries of $CH_3NO_2^-$ and of CH_3NO_2; α denotes the angle between the ONO plane and the CN bond axis from DFT calculations [and from CCSD(t) calculations in parentheses]. The full geometry information is available in Supplementary Information (Ref. 49).

[a]Permanent address: Department of Chemistry, University of Nevada, Reno, 1664 N. Virginia St. MS 216, Reno, NV 89557-0216.
[b]Author to whom correspondence should be addressed. Electronic mail: weberjm@jila.colorado.edu.

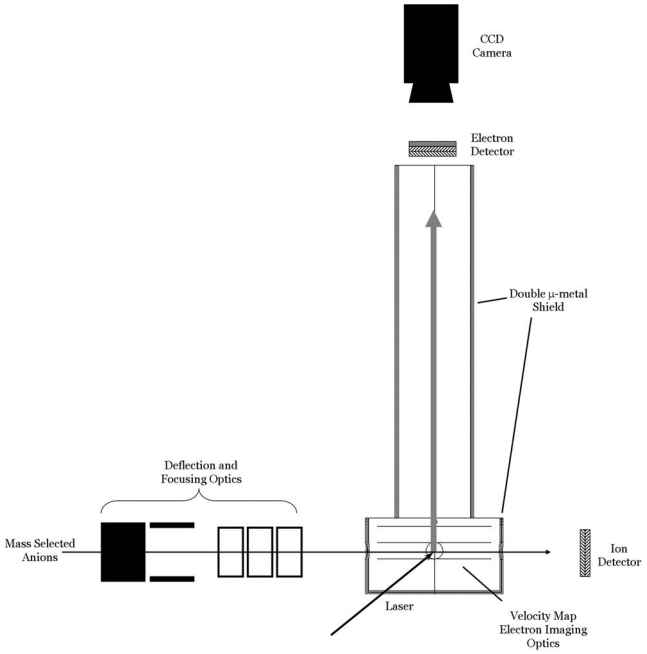

FIG. 2. Schematic of the PE imaging spectrometer (see text).

features in the context of threshold laws for photodetachment and assign the features in the PE spectrum of nitromethane based on FCF calculations.

II. EXPERIMENTAL DETAILS

We use a velocity map imaging PE spectrometer coupled to a time-of-flight (TOF) mass spectrometer, equipped with a supersonic entrainment source for anion generation. The mass spectrometry part of the apparatus has been described in detail before.[11,12] Briefly, we entrain nitromethane vapor through a pulsed valve (General Valve Series 9) into a pulsed supersonic expansion of neat Ar (Even-Lavie Valve, stagnation pressure 13.8 bar). $CH_3NO_2^-$, $CH_3NO_2^- \cdot Ar$, and $CH_3NO_2^- \cdot Ar_2$ anions are formed by attachment of slow electrons to CH_3NO_2 and clusters containing CH_3NO_2 in an electron impact plasma in the high density region of the expansion. The plasma is generated by impact of high energy electrons (800 eV) from an electron beam magnetically confined to the expansion. Anions are mass selected employing a linear TOF spectrometer, and transferred into the detachment region of the velocity map imaging spectrometer by steering ion optics and an Einzel lens (see Fig. 2). The ion beam diameter in the detachment region is about 1 mm.

The velocity map imaging spectrometer is based on the ideas of Eppink and Parker,[13] and its setup is similar to those of the Lineberger and Sanov groups.[14] Photons from a linearly polarized laser beam with its polarization vector parallel to the ion beam detach electrons from the anions in the beam. PE imaging visualizes the probability distribution of PEs in three-dimensional (3D) space. The spatial coordinates of the expanding PE cloud at time t after detachment can be expressed in terms of the electron momentum p in the x, y, and z directions (e.g., $p_x = m_e x/t$). The electrons are accelerated perpendicular to the ion beam into a flight tube. An electrostatic lens is used to image the 3D expanding PE "cloud" that develops upon photodetachment onto a two-dimensional (2D) imaging detector, consisting of a microchannel plate detector coupled to a phosphor screen and a charge coupled device (CCD) camera. Because the linear polarization of the detachment laser is parallel to the plane of detection, the angular distribution of the electrons on the detector is the 2D projection of the 3D PE cloud, where the 3D electron cloud has cylindrical symmetry with the symmetry axis parallel to the laser polarization. The initial 3D distribution of the photodetached electrons can be recovered using an Abel inversion[15] as implemented in the BASEX (Ref. 16) or the pBASEX (Ref. 17) algorithm. The transformed image encodes the electron velocity (or kinetic energy) in the radial PE distribution, and the probability density of photoemission as a function of the emission angle.

The spectrometer is housed in a differentially pumped (turbomolecular pump, 210 ℓ/s) CF150 six-way chamber behind the TOF drift tube, and the reflectron of the mass spectrometry part of the apparatus described in Ref. 11 is switched off. The pressure during operation is on the order of several 10^{-8} mbar. The ion beam is collimated by a 5 mm aperture and focused by an Einzel lens into the detachment region (see Fig. 2). The acceleration stack of the spectrometer itself is made of three oxygen-free, high conductivity (OFHC) copper electrodes, spaced by 15 mm, with 25 mm holes (gridless) in the second and third electrodes to allow the electrons to pass. The total length of the spectrometer is 350 mm. The spectrometer stack including the flight tube is surrounded by two concentric cylinders of annealed μ metal (1 mm wall thickness each) to shield from stray magnetic fields. The electrons are mapped according to their velocities onto a position-sensitive detector, consisting of two microchannel plates (MCPs) (active area of 40 mm) in chevron configuration and a phosphor screen. The MCP detector voltage is gated to enhance our signal-to-noise ratio. The phosphor screen image is digitized by a CCD camera (UNIQ UP-610CL, 659×494 pixels), and the centroids of events in the image are determined and stored using the WENIMAGING program developed in the Suits group.[18] The image is displaced from the center of the phosphor screen because of the ion kinetic energy ($\sim$3.4 keV). As a result, some of the faster PEs that are emitted with velocity components in the ion beam direction may not be registered on the detector. In this case, we use only the half of the image that is fully mapped on the detector after carefully locating the center of the image. Due to symmetry arguments, the complete information on the photoelectron energy and angular distributions is already encoded in each quadrant of the image. While extracting information from one quadrant reduces the signal-to-noise ratio in the resulting photoelectron spectrum, the independent information content in each quadrant is useful for testing the influence of small defects on the position-sensitive detector. In the present experiments, there was a small blind spot on the detector, whose influence on the photoelectron spectra and angular distributions we found to be negligible.

The PE imaging spectrometer is calibrated using the known[19] PE spectrum of S^-, using the second harmonic of a nanosecond-pulsed Nd:yttrium aluminum garnet laser (λ

TABLE I. Frequencies (cm^{-1}) and geometry displacements.

		$CH_3NO_2^-$		CH_3NO_2		$K''/(g/mol)^{1/2}$ Å[a]	
Mode	Assign.[b]	B3LYP[c]	Scaled[d]	B3LYP[c]	Expt.[b]	B3LYP[c]	Fit[e]
1	$w(NO_2)$	411.7	403[f]	616.1	603	0.6802	0.65
2	$\delta_s(CH_3)$	1391.5	1369	1402.9	1380	−0.0428	−0.14
3	$\upsilon_s(NO_2)$	1201.7	1172	1431.9	1397	0.3255	0.34
4	$r_\perp(CH_3)$	1089.6	1084	1136.7	1131	0.1267	0.030
5	$\upsilon(CN)$	844.1	836	926.9	918	−0.2745	−0.31
6	$\delta(NO_2)$	583.8	579	662.5	657	0.0854	
7	$\upsilon_s(CH_3)$	2887.5	2777[g]	3081.6	2974	−0.0345	
8	$\upsilon_s'(CH_3)$	3054.9	2922[g]	3168.4	3045	−0.0034	
9	$\delta_s'(CH_3)$	1461.2	1416	1479.6	1434	0.0122	
10	Torsion	204.2	H.R.[h]	11.6	F.R.[h]	0.0	
11	$r(NO_2)$	446.2	440	481.5	475	0.0	
12	$r_\parallel(CH_3)$	1058.5	1044	1111.4	1096	0.0	
13	$\upsilon_a(NO_2)$	1280.5	1252	1619.0	1583	0.0	
14	$\delta_a(CH_3)$	1472.5	1416	1466.6	1410	0.0	
15	$\upsilon_a(CH_3)$	3108.1	2965[f]	3200.5	3080	0.0	

[a]Geometry displacements in terms of anion normal mode coordinate vectors.
[b]Experimental fundamental frequencies (Ref. 30). Assignment labels in column 2 are taken from Ref. 30.
[c]B3LYP/6-311++G(2*df*,2*p*) harmonic frequencies.
[d]Except as noted, scaled theoretical values as described in the text.
[e]Optimized displacements to fit PE spectrum of Compton *et al.* (Ref. 1).
[f]The experimental value from the present work is (380 ± 56) cm^{-1} as derived from the hot bands (see text).
[g]Experimental fundamental frequencies (Refs. 3 and 5).
[h]H.R., threefold hindered rotor with 953 cm^{-1} barrier from B3LYP/6-311++G(2*df*,2*p*) calculation. F.R., free rotor.

=532 nm). The S^- ions are produced in dissociative electron attachment to CS_2, entrained into the Ar expansion. The typical resolution of the spectrometer is 7.5 meV [full width at half maximum (FWHM)] at 200 meV electron kinetic energy.

PE images of $CH_3NO_2^-$ and $CH_3NO_2^- \cdot Ar$ are obtained by irradiation of the ions with the output of a tunable, nanosecond-pulsed optical parametric converter (LaserVision), operating in the midinfrared (IR, between 2100 and 3800 cm^{-1}, bandwidth ≈ 2 cm^{-1}). The detaching radiation is always polarized parallel to the ion beam and perpendicular to the electron spectrometer axis. The IR beam is passed through Si and Ge filters to remove traces of pump radiation and of the idler radiation produced in the optical parametric converter. Immediately before entering the apparatus, the IR beam passes a Si polarizer to clean up the polarization. Likewise, the 532 nm beam used for calibration is passed through a polarizer immediately before entering the apparatus. While images are already interpretable with as few as several 10^5 events, typical images contain several 10^6 events. The corresponding acquisition time varies depending on laser fluence and ion intensity, but typical acquisition times are on the order of 30 min to one hour for good signal-to-noise ratio.

III. COMPUTATIONAL DETAILS

A. *Ab initio* calculations

Computational chemistry calculations were performed using the GAUSSIAN 03 program.[20] Geometries and frequencies for $(^2A')$ $CH_3NO_2^-$ and $(^1A')$ CH_3NO_2 were calculated using density functional theory (DFT) with the Becke-3 Lee–Yang–Parr (B3LYP) hybrid functional[21] and the 6-311++G(2*df*,2*p*) basis set.[22] Geometries were also calculated using coupled-cluster theory with single and double excitations and perturbative inclusion of triples (CCSD(T)) (Ref. 23) with the aug-cc-pVTZ basis set.[24] The anion and neutral geometries for the two levels of theory are shown in Fig. 1. The most significant geometry deviation between the DFT and coupled-cluster calculations is in the angle α between the plane of the NO_2 group and the CN bond. Calculated DFT frequencies are provided in Table I. The calculated electron affinity is $EA_0(CH_3NO_2)=0.162$ eV at the CCSD(T)/aug-cc-pVTZ level with vibrational zero-point energy corrections from the B3LYP/6-311++G(2*df*,2*p*) harmonic frequencies. Detailed computational results are provided in the Supplementary Information.[49]

B. Franck–Condon analysis

Vibrational normal modes from the DFT calculations were employed to simulate the Franck–Condon profiles using the PESCAL program.[25,26] Except for the torsional vibration for internal rotation around the CN bond, which is discussed separately in Sec. IV C, the FCFs were calculated in the independent harmonic oscillator approximation with full treatment of the Duschinsky rotation[27] of the normal mode eigenvectors between the anion and neutral, using the Sharp–Rosenstock–Chen recursion method.[25,28,29] Additional details of the Franck–Condon simulations described here are provided in the Supplementary Information.[49]

The vibrational frequencies for neutral CH_3NO_2 (14 of the 15 modes, i.e., excluding the torsion) were taken from the experimental infrared/Raman fundamental frequencies[30] and substituted for the calculated values. The three CH

stretch fundamental frequencies for the anion were taken from infrared spectroscopy experiments.[3,5] The other anion frequencies were estimated by scaling the calculated B3LYP/6-311++G($2df$,$2p$) harmonic values by the ratio of the experimental fundamental to calculated harmonic frequency of the neutral for the similar normal mode. These frequencies are given in Table I.

Both anionic and neutral CH_3NO_2 have C_s planar symmetry with nine totally symmetric vibrational modes (which have nonzero normal coordinate displacements between the anion and neutral) and six nontotally symmetric modes (zero displacements). Nontotally symmetric modes are considered Franck–Condon "inactive," but can have some activity for $2n \leftarrow 0$ transitions because of the overlap of the even wave functions with different harmonic frequencies. All $n \leftarrow 0$ transitions are possible with nonharmonic potentials (e.g., the torsional mode). The calculated geometry changes between the anion and neutral are given in Table I, presented as the $\vec{K}''$ displacement vector in the anion normal coordinate frame as defined elsewhere.[25,29] The signs of the Cartesian displacement vectors are arbitrary in the harmonic oscillator approximation, but need to be defined self-consistently for the Duschinsky rotation calculations. We have chosen the direction of the normal coordinates for each mode such that the B rotational constant of the molecule decreases (I_{yy} component of the moment of inertia increases) for a positive displacement.

The internal rotation of the methyl and NO_2 groups about the CN bond is a hindered rotor in the anion but is essentially a free rotor in neutral CH_3NO_2. The torsional potentials are calculated at the B3LYP/6-311++G($2df$,$2p$) level by scans of the HCNX dihedral angle, where X is a dummy atom placed 90° to the CN bond and defining the bisector of the NO_2 group, while all other distances and angles are allowed to relax. For the anion, the potential energy is well approximated by a cosine function,

$$V(\varphi) = (V_0/2)(1 - \cos n\varphi),$$

with $n=3$ and a barrier of $V_0=953$ cm^{-1}. For the neutral, the potential is sixfold symmetric and nearly a free rotor with a barrier of less than 2 cm^{-1}. The vibrational wave functions and energy levels for the torsions were calculated as described by Spangler[31] by solving the one-dimensional Schrödinger equation with a free-rotor basis set. The reduced moments of inertia were obtained as $I_r=(1/I_{CH_3}+1/I_{NO_2})^{-1}$ with the CH_3 and NO_2 group moments of inertia obtained from the calculated geometries relative to the CN bond axis. This is the simplest approximation for the rotor moment of inertia as described by East and Radom.[32] The neutral is treated as a free internal rotor.

The calculation of Franck–Condon factors for torsional vibrations has been outlined by Ingham and Strickler[33] and by Spangler and Pratt.[34] For the present case, where the cosine potential functions of the upper and lower states are in-phase (minima at the same configuration), the Franck–Condon overlaps are a simple sum over the coefficients of the free-rotor basis functions forming the torsional wave functions. A standalone FORTRAN program was developed to calculate the Franck–Condon factors for torsional modes and the resulting transition intensities were imported into PESCAL.[26] This effectively treats the torsional mode as an independent oscillator with no Duschinsky mixing with other modes, which is a good approximation because the torsion is a nontotally symmetric mode.

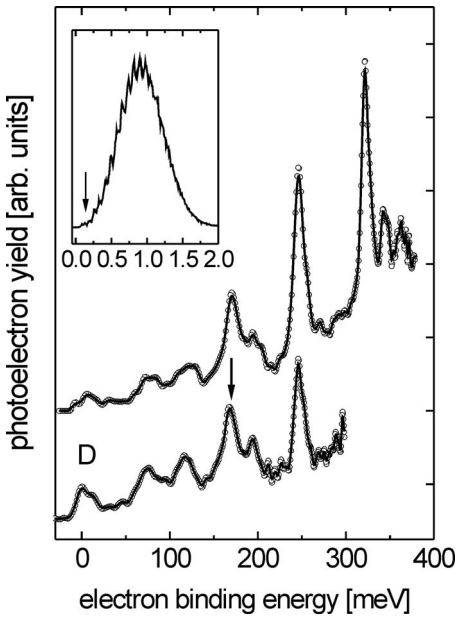

FIG. 3. PE spectra of $CH_3NO_2^-$ at 322 meV (2600 cm^{-1}, lower trace), 397 meV (3200 cm^{-1}, upper trace), and from Ref. 1 (inset, abscissa is in units of eV); the circles are data points, the full lines are five point adjacent averages to guide the eye; the arrow denotes the peak corresponding to the vibrational ground state of the neutral molecule (AEA=172±6 meV), D the signature of the dipole-bound state.

IV. RESULTS AND DISCUSSION

A. Interpretation of the photoelectron spectrum, adiabatic electron affinity determination, and the dipole-bound state

The uncertainty in the AEA determination of Compton *et al.*[1] was due to the shape of the PE spectrum, which is dominated by an extended vibrational progression, peaking at a vertical detachment energy of about 0.9 eV. The AEA determination was done by using the last discernible peaks at the low binding energy side of the spectrum.

Figure 3 shows the PE spectra of $CH_3NO_2^-$ at 397 meV (3200 cm^{-1}) and 322 meV (2600 cm^{-1}) photon energy, and a sample photoelectron image is presented in Fig. 4. This corresponds to the low binding energy side of Compton's *et al.* spectrum (inset in Fig. 3). The spectrum is dominated by a progression of intense peaks with a spacing of (76±7) meV or (613±56) cm^{-1} The lower binding energy range shows a series of smaller features with less regular spacing. We note that all photon energies in this study were chosen carefully to avoid the influence of known vibrational autodetachment resonances of the $CH_3NO_2^-$ anion.[3,5]

At this point, we can tentatively assign the three intense features as the main vibrational progression, with the vibrational 0-0 origin transition at the nominal peak position of $E_B=(170\pm5)$ meV, and the features toward lower binding energies as hot bands. The energy spacing of

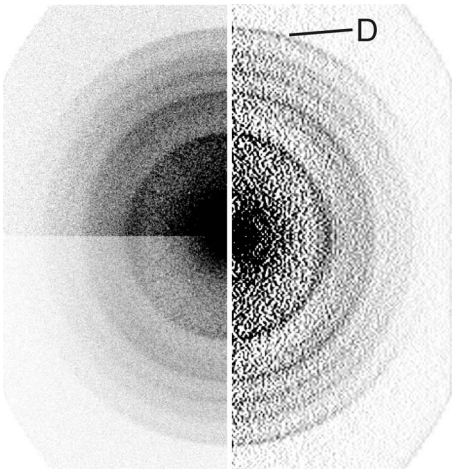

FIG. 4. PE image of $CH_3NO_2^-$ at 322 meV (2600 cm^{-1}) photon energy, based on one quadrant of the raw photoelectron image (see Sec. II). The left half of the figure contains the raw PE image with the intensity in the upper portion doubled to better show the dynamic range of the image without saturating the gray scale. The right half of the figure shows the BASEX transformed image with the "center line artifact" from the BASEX transformation removed. The signature belonging to the dipole-bound state has been labeled "D."

(613 ± 56) cm^{-1} is in agreement with the value of (645 ± 70) cm^{-1} or (80 ± 9) meV reported by Compton *et al.*[1] and corresponds to the 603 cm^{-1} frequency for the NO_2 wag mode of gas-phase CH_3NO_2 reported by Gorse *et al.*[30] The comparison of the spectrum of bare $CH_3NO_2^-$ and that of $CH_3NO_2^- \cdot Ar$ (see Fig. 5) corroborates this assignment. The series of intense peaks spaced by 76 meV is shifted by (63 ± 7) meV toward higher binding energies upon Ar solvation. The hot bands at lower binding energies are suppressed for $CH_3NO_2^- \cdot Ar$ because of the much lower internal energy of the Ar complex (see below). The photoelectron spectrum of $CH_3NO_2^- \cdot Ar_2$ (not shown) is shifted by an additional (61 ± 7) meV relative to that of $CH_3NO_2^- \cdot Ar$. This very regular behavior in the Ar induced shifts confirms our identification of the hot bands in the spectrum of bare $CH_3NO_2^-$. Therefore, we determine the AEA of CH_3NO_2 to be (172 ± 6) meV (after corrections for torsional and rotational contour shifts discussed below).

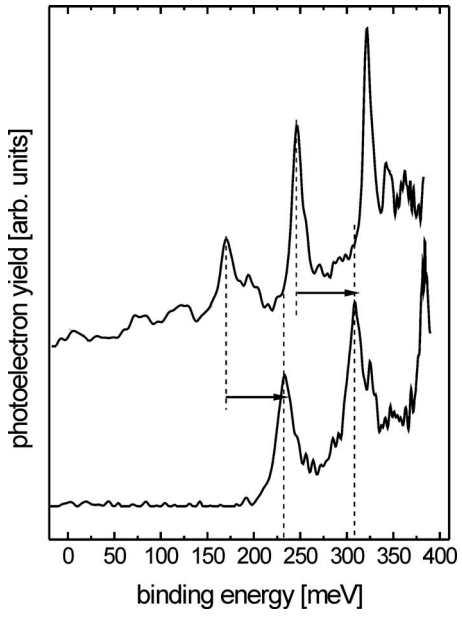

FIG. 5. PE spectra of $CH_3NO_2^-$ (upper trace) and $CH_3NO_2^- \cdot Ar$ (lower trace) at 397 meV (3200 cm^{-1}) photon energy. The dashed lines and arrows show how the vibrational progression of the neutral molecule shifts by 63 meV toward higher binding energies upon solvation by one Ar atom.

Comparing the geometries of anionic and neutral CH_3NO_2, we note that the most prominent geometry difference between the two charge states is the position of the NO_2 group relative to the CN bond. This difference likely will lead to an extended vibrational progression with large FCF in the photoelectron spectrum. Based on this assumption, we can already at this point tentatively assign the most intense peaks in the experimental PE spectrum of $CH_3NO_2^-$ at 397 meV (3200 cm^{-1}) photon energy as the first three members of a progression of the neutral NO_2 wagging mode $\nu_1^{(0)}$ (see Table I for the labeling of the modes) with quantum numbers $n_1^{(0)}=0$, 1, and 2. In addition, we can identify a peak at (122 ± 5) meV binding energy as a hot band of the anionic NO_2 wagging mode $\nu_1^{(-)}$, i.e., corresponding to the transition $n_1^{(0)}=0 \leftarrow n_1^{(-)}=1$ and a peak at (77 ± 5) meV as a hot band in the same mode, but with quantum numbers $n_1^{(0)}=0 \leftarrow n_1^{(-)}=2$. We therefore arrive at an experimental frequency for the anionic NO_2 wagging mode of (380 ± 56) cm^{-1}. A band at (195 ± 5) meV binding energy is the signature of the transition $n_1^{(0)}=1 \leftarrow n_1^{(-)}=1$. The higher members of this progression are very weak, but observable as shoulders on the high energy sides of the intense neutral progression. We note that other low-frequency modes may contribute to the observed hot bands. We will discuss the assignment of the observed vibrational features based on calculated FCF below (see Sec. IV C).

The PE spectra of bare $CH_3NO_2^-$ show a weak feature at a binding energy of (8 ± 8) meV. This feature does not correspond to any of the possible anion vibrational modes with any appreciable Franck–Condon intensity (see below), which makes it highly unlikely to be a hot band. Compton *et al.*[1] determined the binding energy of the dipole-bound state of $CH_3NO_2^-$ populated in Rydberg electron transfer experiments to be (12 ± 3) meV, in agreement with the feature we observe in the PE spectrum. We tentatively assign this feature at low binding energies to the dipole-bound state of $CH_3NO_2^-$, which has not been observed previously by PE spectroscopy. A proof of this assignment would be the observation of this feature in the PE spectrum of $CH_3NO_2^- \cdot Ar$. However, the dipole-bound state seems to be strongly suppressed in $CH_3NO_2^- \cdot Ar$, and its signature is not intense enough to create a peak significantly above the noise level in the corresponding PE spectrum (see Fig. 5). This behavior might suggest it to be a hot band. However, the anisotropy of the photodetached electrons from this feature (taken at several photon energies) does not fall into the same trend as those from the clearly valence-bound hot bands, hinting at a different electronic state involved, as will be discussed in Sec. IV B.

B. Photoelectron angular distributions

PE angular distributions $f(\theta)$ from photodetachment by linearly polarized light as a function of the emission angle θ with respect to the polarization axis can be described using the expression[35,36]

$$f(\theta) = \frac{\sigma_0}{4\pi}[1 + \beta(\ell, E_K)P_2(\cos\theta)], \quad (1)$$

where σ_0 is the total detachment cross section, $P_2(\cos\theta) = (1/2)(3\cos^2\theta - 1)$ is the second order Legendre polynomial in $\cos\theta$, and β is the anisotropy parameter (in older parts of literature also known as asymmetry parameter), ranging from $\beta = -1$ (emission predominantly perpendicular to polarization vector) to $\beta = +2$ (emission predominantly parallel to polarization vector). β depends on the orbital angular momenta of the contributing partial waves and on the kinetic energy E_K of the emitted electron. E_K is connected to the electron binding energy E_B by

$$E_B = h\nu - E_K. \quad (2)$$

The PE spectra of atoms can often be described by linear combinations of only a few partial waves that contribute significantly to the PE angular distributions, because of the high symmetry of atomic orbitals. For photodetachment from molecules, however, the often complicated shapes of molecular orbitals generate contributions from high angular momentum partial waves. At low electron kinetic energies E_K, however, the relative weights of these partial waves are governed by Wigner's threshold law,[37] stipulating that the relative cross section σ_ℓ of a partial wave with given orbital angular momentum ℓ behaves as

$$\sigma_\ell \propto E_K^{\ell+1/2}. \quad (3)$$

As s waves (i.e., $\ell = 0$) are isotropic ($\beta = 0$), and dominate at low kinetic energies over the contributions of partial waves with higher orbital angular momentum, we expect the anisotropy parameter to progressively deviate from $\beta = 0$ as E_K increases. For a given electronic final state, the variation of β with energy is expected to be monotonic and smooth. Inspecting the experimental results for $CH_3NO_2^-$ (see Fig. 6), we observe that the values of the anisotropy parameter for the valence states (including the hot bands) follow a consistent trend, increasing from $\beta \approx 0$ (outgoing s-wave) at low E_K to $\beta \approx 1.25$ for $E_K \approx 325$ meV. This is consistent with the contribution from the s partial wave dominating at low kinetic energies, while higher angular momenta play an increasing role as E_K increases. We caution that Wigner's threshold law strictly only holds for electron-molecule interaction potentials that fall off faster than $1/r^2$. Interactions with polar molecules, especially those with a dipole moment sufficiently large to support a bound state, can behave stepwise and oscillatory.[38]

In contrast to the valence state (including the hot bands), photodetachment from the dipole-bound state results in $\beta \approx 2$ for all data points corresponding to this state for all photon energies (see Fig. 6). This dramatic difference confirms that the electrons in this feature originate from a different electronic state than the electronic ground state of the anion. Moreover, the large β value is consistent with a nearly pure p character of the outgoing wave, similar to photodetachment from H^- ions,[36,39] resulting from photodetachment out of an s-like orbital. The dipole-bound state is expected to be spatially extended and s-like in shape. This is consistent with our observations along the lines of this simple argument. We note, however, than an outgoing p-wave is not the only possibility to generate an anistropy parameter $\beta \approx 2$. Moreover, the presence of a strong dipole moment can also modify the predicted anisotropy parameters from this simple expectation.[40]

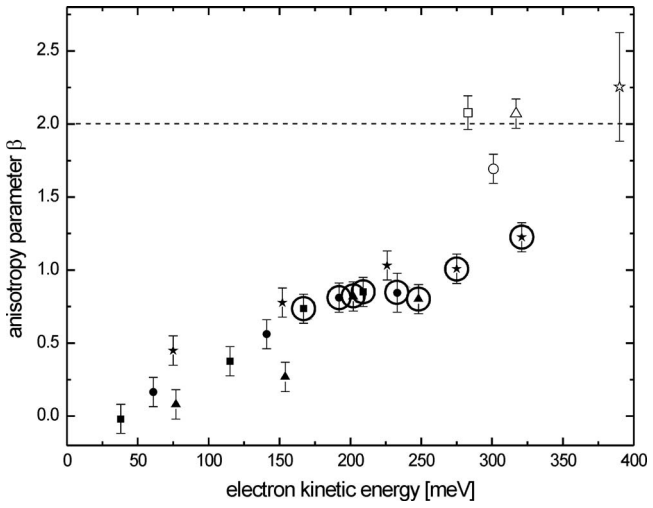

FIG. 6. Anisotropy parameters as a function of electron kinetic energy for different photon energies. Squares, circles, triangles, and stars correspond to data taken at 2300, 2500, 2600, and 3200 cm^{-1}, respectively. Filled symbols correspond to the valence electronic state, while the open symbols belong to the dipole-bound state. The data points marked with larger circles belong to the hot bands at binding energies of 77 and 122 meV. Error bars have been conservatively estimated to be ± 0.1, except in cases where the fits of the angular distributions to Eq. (1) resulted in larger error bars because of poorer signal-to-noise ratios. The dashed line shows the theoretical maximum of the value for the anisotropy parameter ($\beta = 2$).

C. Franck–Condon analysis of the PE spectrum of $CH_3NO_2^-$

In the photodetachment transition from $CH_3NO_2^-$ to CH_3NO_2, the largest geometry displacement is along the NO_2 wagging normal coordinate with the known frequency[30] of 603 cm^{-1} in the neutral. As discussed above, this mode accounts for the major Franck–Condon active progression in the photoelectron spectrum according to the simulation based on the DFT calculations. Four other modes, listed as modes 2–5 in Table I, also show substantial Franck–Condon activity, primarily for their $1 \leftarrow 0$ and $2 \leftarrow 0$ transitions. Together, these five modes account for over 90% of the Franck–Condon profile intensities. Combination bands involving modes 3–5 with frequencies of 1100–1300 cm^{-1} tend to overlap with the transitions from the NO_2 wagging at moderate resolution, causing shifts in the observed peaks. That accounts for the observed spacing of 645 cm^{-1} reported by Compton *et al.*[1]

As a consequence of the differences in geometry between anion and neutral, the character of the internal rotation of the methyl group changes completely upon electron de-

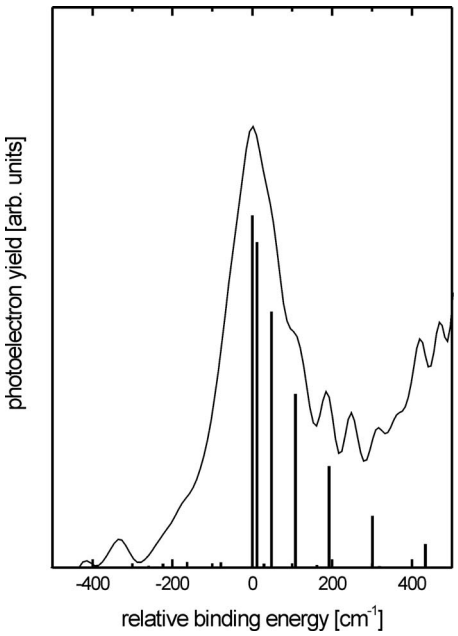

FIG. 7. Comparison of the torsional FCF calculation (vertical sticks) at 100 K temperature and the experimental results for $CH_3NO_2^- \cdot Ar$, shifted by the EA of the Ar complex (full line).

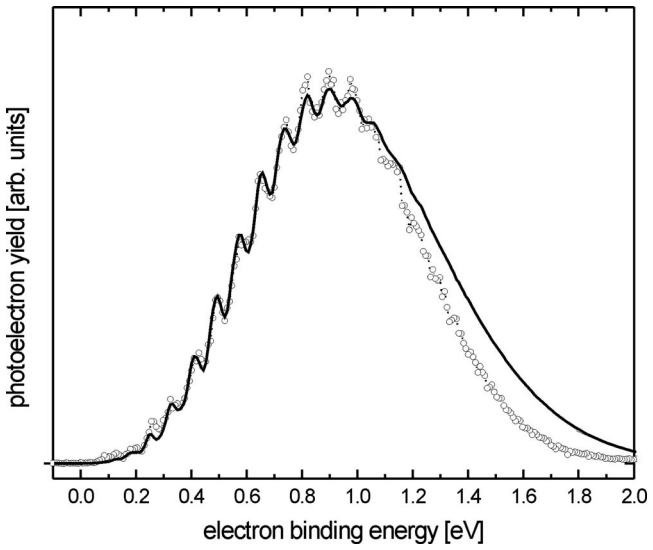

FIG. 8. Comparison of the experimental photoelectron spectrum by Compton *et al.* (Ref. 1) with a fitted FCF simulation (see text).

tachment. In the anion, the methyl rotor is strongly hindered, while it is essentially a free rotor in the neutral. This leads to each vibrational band being accompanied by combination bands involving the hindered-to-free rotor transitions. Figure 7 shows the simulated spectrum for $CH_3NO_2^-$ at 100 K in comparison with the experimental PE spectrum of $CH_3NO_2^- \cdot Ar$ at a photon energy of 322 meV (2600 cm^{-1}). We chose this particular ion because its PE spectrum will be virtually free of hot bands, as it should be quite cold. While the individual transitions are not resolved in the experimental spectrum, the shape of the $0 \leftarrow 0$ band is clearly asymmetric with a steeper low binding energy slope. On the basis of our FCF calculations, we argue that this asymmetry is mainly due to the hindered-to-free methyl rotor transitions. A stick spectrum of the Franck–Condon transitions for the torsional mode is shown in Fig. 7. Because the upper state is a near-free rotor and the lower state hindered rotor ground-state wave function includes components of a series of free-rotor basis set functions that overlap with the free-rotor wave functions, the simulated spectrum is qualitatively reminiscent of rotational structure. In the independent oscillator approximation, this structure is repeated for every vibrational transition in the nitromethane spectrum. At the available experimental resolution, the individual torsional transitions are not resolved but they contribute to the broadening of the observed transitions.

Rotational contours were calculated as described previously[41,42] using the DFT geometries and treating the anion and neutral as asymmetric tops. At the experimental resolution, the rotational contours are only slightly asymmetric and the peak shift is -1.2 meV at 250 K. However, the contour due to the internal torsional transitions shifts the peaks in the opposite direction. Simulation of both the torsional and rotational transitions (both calculated for 250 K and using an instrumental resolution of 7.5 meV) gives a net shift of $(+2 \pm 1)$ meV This shift has been accounted for in the electron affinity values reported above.

Because the low-energy imaging photoelectron spectra exhibit only the first few transitions of the Franck–Condon envelope, Franck–Condon fits where the geometry displacements are optimized are not well constrained by the present experiments. In addition, variations in the photodetachment cross sections are expected owing to threshold effects for imaging spectra taken at low photon energies. Therefore, we first compare the Franck–Condon simulations to the $CH_3NO_2^-$ photoelectron spectrum of Compton *et al.*,[1] which was taken at a photon energy of 2.54 eV and exhibits the entire Franck–Condon band profile. Figure 8 compares the experimental spectrum with Franck–Condon simulations using normal coordinates from the DFT calculations, frequencies given in Table I, and the origin assignment as obtained from our imaging experiments. The peaks are convolved by a Gaussian function with a FWHM of 30 meV as reported for the instrumental resolution.[1] An anion vibrational temperature of 300 K is assumed. The raw calculated displacements already gave a very good match with the experimental spectrum, but the displacements for the first five modes, the electron affinity, and a scaling factor were optimized to provide a least-squares fit to the experiment over the electron binding energy range of 0–1.3 eV. The optimized displacements are given in Table I. The changes from the calculated displacements are minor and should be considered as qualitative values because individual transitions for the five optimized modes are not resolved in the experiment. Additional details of the simulation are provided in the Supplementary Information.[49] The optimized electron affinity is 168 meV, in good agreement with the imaging result of (172 ± 6) meV. As shown in Fig. 8, the simulation provides an excellent fit to the experimental photoelectron spectrum, especially considering that anharmonicity effects are not included, even though the progression of the NO_2 wagging mode extends to fairly high vibrational levels. This agreement confirms that

the photoelectron spectrum of Compton *et al.*[1] is consistent with our origin assignment from low-energy photoelectron imaging. As indicated by Compton *et al.*,[1] however, their spectrum alone is insufficient for a definitive assignment of the origin. Indeed, we could also produce reasonable Franck–Condon fits with assignments of EA ≈ 20, 95, or 245 meV. Therefore, the higher-resolution and lower-temperature imaging experiments are essential for determining a precise electron affinity.

For the present purposes, we now have a validated set of Franck–Condon intensity parameters constrained to match the full experimental photoelectron spectrum.[1] These may be used to compare Franck–Condon simulations with the present experiments. A minor complication is that the imaging spectra are acquired in the velocity domain, rather than as a function of electron kinetic energy (E_K) for conventional photoelectron spectroscopy.[1,43] The instrumental resolution function has constant width in velocity space but varies as $E_K^{1/2}$ after the spectra are converted to E_K or electron binding energy, $E_B = h\nu - E_K$. To account for these effects properly, PESCAL (Ref. 26) has been modified to calculate and fit photoelectron spectra in the original velocity space (or time space for time-of-flight techniques), then perform the appropriate Jacobian transformation of both the data and the simulation afterward to convert to electron binding energies for presentation.

Because the imaging spectra are taken at near-threshold photon energies, it is also necessary to consider the dependence of the photodetachment cross section on photoelectron velocity, which can modify the Franck–Condon intensities. According to the Wigner threshold law (2), the photodetachment probability is proportional to $E_K^{\ell+1/2}$ where $\ell = 0$ for *s*-wave electron detachment (removal from a *p*-electron orbital at low kinetic energy), $\ell = 1$ for *p*-wave (removal of an *s*-electron), etc. Above threshold, interference effects can be observed, for example, between *s*- and *d*-electron waves for detachment from a *p*-orbital.[35,36] The situation is considerably more complex for detachment from molecular orbitals. Reed *et al.*[42] and Clodius *et al.*[45] applied theoretical methods in a single-electron approximation to calculate the photodetachment intensity for molecules as a function of photon energy above the threshold. Unfortunately, there is no simple or general functional form for the velocity dependence for molecular anion photodetachment intensities, as it depends on the details of the interference of outgoing electron waves from molecular orbitals arising from a mixture of atomic orbitals on different centers. Nevertheless, some general considerations apply (neglecting the influence of the dipole moment of the neutral molecule): (1) First, the leading term for the velocity dependence is proportional to $E_K^{1/2}$. This electron velocity factor appears in the coefficient of the expressions for atomic negative ion photodetachment cross sections given by Massey,[46] for molecular photodetachment by Reed *et al.*,[44] and was cited by Ervin and co-workers[42,47] as appropriate for scaling Franck–Condon factors in photoelectron spectroscopy simulations. Because $E_K^{1/2}$ gives a relatively slow variation at moderate electron kinetic energies E_K, this factor usually has a very minor effect on the simulation of FCF for conventional negative ion photoelectron spectroscopy, i.e., for photon energies in the 2–4 eV range and electron kinetic energies greater than 0.3 eV over the energy range of typical vibronic transitions. The $E_K^{1/2}$ scaling factor is exact for pure *s*-wave detachment and will predominate over higher-order terms very near threshold. However, scaling proportional to $E_K^{1/2}$ is incorrect in general when detachment involves higher-order electron waves with possible interference effects. Pure *p*-wave detachment (or higher-order spherical harmonics) with $E_K^{3/2}$ dependence (or higher powers) can become relevant at slightly higher kinetic energies, until the detachment behavior is no longer governed by Wigner's law. Detailed evaluation of the photodetachment matrix elements as a function of photon energy and averaging over molecular orientations is required for a complete treatment.[44,45] (2) Second, Reed *et al.*[44] introduced the principle of comparing the overall group symmetry of the highest occupied molecular orbital (HOMO) from which the electron is detached to atomic orbital symmetry to assign the predominant near-threshold electron detachment symmetry. For the present case, the HOMO of $CH_3NO_2^-$ is an A' orbital centered on the NO_2 group composed predominantly of *p*-orbitals pointing out of the ONO plane with the same phase on the O atoms and the opposite phase on the N atom. The orbital is pictured in Fig. 9; in the pseudoatomic limit the HOMO exhibits *d*-like symmetry with two angular nodes (one in the ONO plane and one passing between the N atom and the two O atoms). That would imply that the detachment would result in a *p*-wave as a first-order approximation. However, the HOMO also includes other atomic orbital components with smaller coefficients, which will complicate this picture. (3) Third, the angular distribution of the photodetachment relative to the electric field vector of the laser provides complementary information regarding the symmetry of the photodetached electron wave. In the present case, the detachment at the lowest electron velocities exhibits isotropic *s*-wave behavior ($\beta \approx 0$) as shown in Fig. 6, which implies $\ell = 0$, but β increases with increasing photoelectron velocities suggesting that higher-order terms become important.

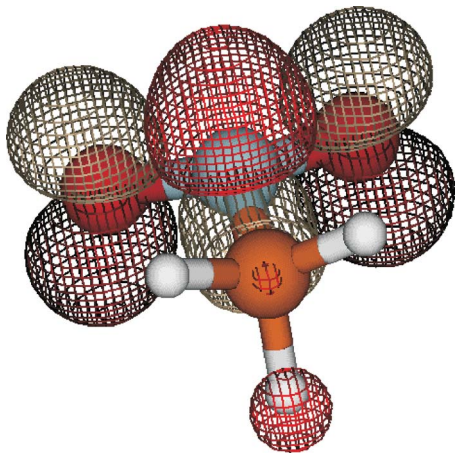

FIG. 9. (Color online) HOMO of $CH_3NO_2^-$. The HOMO is mainly localized on the nitro group, but small parts also permeate into the rest of the molecular frame, even the σ^* antibonding orbital of the CH group *syn* to the nitro group.

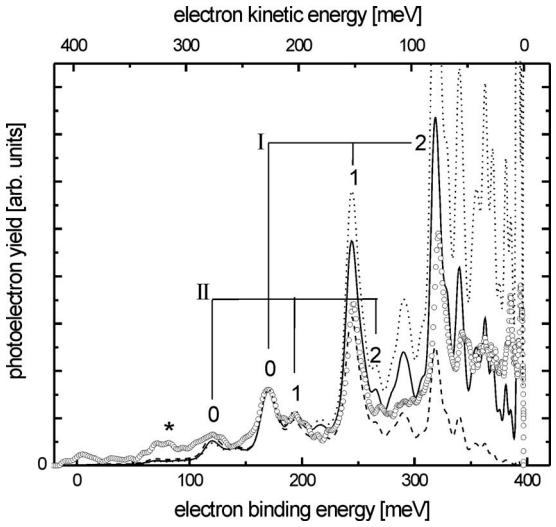

FIG. 10. FCF fits to the experimental photoelectron spectrum of $CH_3NO_2^-$ (open circles) at 397 meV (3200 cm^{-1}) with no velocity scaling (dotted line), scaled with $E_K^{1/2}$ (pure *s*-wave, full line), and scaled with $E_K^{3/2}$ (pure *p*-wave, dashed line); see text for more details. The sequences marked in the spectrum are based on the NO_2 wagging mode ν_1 with transitions $n \leftarrow 0$ (series I) and $n \leftarrow 1$ (series II). The asterisk marks the $0 \leftarrow 2$ hot band of the NO_2 wagging mode. Note that the top scale shows the electron kinetic energy, while the bottom scale gives the electron binding energy.

Experimental evidence shows that near-threshold low-electron-velocity detachment transitions in imaging experiments are indeed suppressed compared to Franck–Condon intensities. For example, Surber and Sanov[48] noted the diminution of near-threshold transitions compared to Franck–Condon intensities in the CS_2^- imaging photoelectron spectrum. This effect is also evident in the present experiments, as may be seen by comparing the relative intensities of the $0 \leftarrow 0$ and $1 \leftarrow 0$ NO_2 wagging transitions in the spectra in Fig. 3 taken at two different photon energies. The $1 \leftarrow 0$ transition has lower relative intensity in the spectrum that was taken at lower photon energy and therefore closer to threshold.

The imaging spectrum at 397 meV photon energy (3200 cm^{-1}) is compared to Franck–Condon simulations in Fig. 10. Three simulations are shown, one without electron velocity scaling (simple Franck–Condon approximation), one scaled by $E_K^{1/2}$ (pure *s*-wave detachment), and one scaled by $E_K^{3/2}$ (pure *p*-wave detachment). Comparing the simulation without velocity scaling, it is obvious that transitions at low electron velocity (high electron binding energy) are strongly suppressed. The simulations that are scaled by $E_K^{1/2}$ or $E_K^{3/2}$ better match the relative intensities of the observed spectrum, but neither is an exact fit over the whole energy range. That behavior suggests that a more sophisticated calculation of the photodetachment cross sections as a function of photoelectron velocity including multiple terms would be required to match the experimental intensities. Nevertheless, the overall match between the experimental spectrum and the simulations is sufficient to verify the assignments of the transitions discussed above.

The intensity of the hot band assigned in Fig. 10 as the $0 \leftarrow 2$ ($E_B \approx 77$ meV) transition of the NO_2 wagging mode is about a factor of four higher than predicted by the Franck–Condon simulations. The simulations in Fig. 10 use an anion temperature of 250 K, which roughly reproduces the relative intensities of the $0 \leftarrow 0$ origin and nearby $1 \leftarrow 1$ sequence band of the wagging mode. At this temperature, the observed intensity of the $0 \leftarrow 2$ band is too high relative to the $0 \leftarrow 1$ and $0 \leftarrow 0$ transitions to be explained by a Boltzmann distribution. However, if the anion vibrational temperature is increased to 400 K to match the $0 \leftarrow 2$ hot band intensity, then the intensities of the $n \leftarrow 2$ transitions for $n=1$, 2, and 3 are too strong compared to the experiment. The source of this intensity discrepancy is uncertain—anharmonicity effects could be partly responsible. The disappearance of the peak in the cold $CH_3NO_2^- \cdot Ar$ spectrum (Fig. 5) and the fact that its anisotropy follows the same trend as the main progression (Fig. 6) imply, however, that this feature is indeed due to hot bands and is unrelated to the dipole-bound state (peak *D* in Fig. 3). Finally, we note that the two vibrational hot bands predicted to be nearest the dipole-bound detachment peak at $E_B=(8 \pm 8)$ meV are a $0 \leftarrow 3$ NO_2 wag transition at -1209 cm^{-1} or $E_B=19.1$ meV and a combination of $0 \leftarrow 1$ in the NO_2 wag and $0 \leftarrow 1$ in the CN stretch at -1239 cm^{-1} or $E_B=15.4$ meV. Even allowing for frequency shifts (and ignoring the distinctive anisotropy of peak *D*), the calculated Franck–Condon intensities of these hot bands are each less than 0.3% of the 0-0 origin peak, much too small to account for the observed feature.

V. SUMMARY AND CONCLUSIONS

We have studied the photoelectron energy spectra and angular distributions for low-energy photodetachment of nitromethane anions. We have determined a new and more accurate value of the adiabatic electron affinity of nitromethane of (172 ± 6) meV, and we were able to unambiguously assign many of the vibrational features in the photoelectron spectrum. The most intense peaks observed in the photoelectron spectrum are due to progressions of the neutral NO_2 wagging mode. We observe the dipole-bound state of the nitromethane anion, clearly identifiable through its anisotropy, which is very different from the valence state based vibrational features. We postulate the existence of bound-to-free transitions of the internal methyl rotor, which are unresolved in the present photoelectron spectra, but are the cause for an asymmetry in the prominent vibrational features, and contribute strongly to the spectral congestion of the photoelectron spectra. Future high resolution photoelectron spectroscopy experiments at even lower photon energies may be able to resolve these features.

ACKNOWLEDGMENTS

We gratefully acknowledge the National Science Foundation for financial support through the JILA Physics Frontier Center (NSF Grant No. PHY-0551010). We thank K. H. Bowen for providing the PE spectrum of $CH_3NO_2^-$ in digital form. We thank W. C. Lineberger, L. Sheps, E. M. Miller, M. A. Johnson, and L. R. McCunn for helpful discussion. K.M.E. acknowledges funding from the Department of

Energy, Office of Basic Energy Sciences, Chemical Sciences, Biosciences and Geosciences Division, a JILA Visiting Fellowship, and sabbatical support from the University of Nevada, Reno.

[1] R. N. Compton, H. S. Carman, C. Desfrancois, H. Abdoul-Carime, J. P. Schermann, J. H. Hendricks, S. A. Lyapustina, and K. H. Bowen, J. Chem. Phys. **105**, 3472 (1996).
[2] F. Lecomte, S. Carles, C. Desfrancois, and M. A. Johnson, J. Chem. Phys. **113**, 10973 (2000); L. Suess, R. Parthasarathy, and F. B. Dunning, *ibid.* **119**, 9532 (2003).
[3] J. M. Weber, W. H. Robertson, and M. A. Johnson, J. Chem. Phys. **115**, 10718 (2001).
[4] A. Modellia and M. Venuti, Int. J. Mass Spectrom. **205**, 7 (2001); I. C. Walker and M. A. D. Fluendy, *ibid.* **205**, 171 (2001); W. Sailer, A. Pelc, S. Matejcik, E. Illenberger, P. Scheier, and T. D. Mark, J. Chem. Phys. **117**, 7989 (2002); C. Q. Jiao, C. A. DeJoseph, and A. Garscadden, J. Phys. Chem. A **107**, 9040 (2003); E. Alizadeh, F. F. da Silva, F. Zappa, A. Mauracher, A. Probst, S. Denifl, A. Bacher, T. D. Mark, P. Limao-Vieira, and P. Scheier, Int. J. Mass Spectrom. **271**, 15 (2008).
[5] H. Schneider, K. M. Vogelhuber, F. Schinle, J. F. Stanton, and J. M. Weber, J. Phys. Chem. A **112**, 7498 (2008).
[6] G. L. Gutsev and R. J. Bartlett, J. Chem. Phys. **105**, 8785 (1996); T. Sommerfeld, Phys. Chem. Chem. Phys. **4**, 2511 (2002).
[7] G. L. Gutsev, P. Jena, and R. J. Bartlett, J. Chem. Phys. **110**, 403 (1999).
[8] C. E. H. Dessent, J. Kim, and M. A. Johnson, Faraday Discuss. **115**, 395 (2000).
[9] A. Osterwalder, M. J. Nee, J. Zhou, and D. M. Neumark, J. Chem. Phys. **121**, 6317 (2004).
[10] J. H. Hendricks, H. L. de Clercq, C. B. Freidhoff, S. T. Arnold, J. G. Eaton, C. Fancher, S. A. Lyapustina, J. T. Snodgrass, and K. H. Bowen, J. Chem. Phys. **116**, 7926 (2002).
[11] J. M. Weber and H. Schneider, J. Chem. Phys. **120**, 10056 (2004).
[12] H. Schneider, K. M. Vogelhuber, and J. M. Weber, J. Chem. Phys. **127**, 114311 (2007).
[13] D. H. Parker and A. Eppink, J. Chem. Phys. **107**, 2357 (1997); A. Eppink and D. H. Parker, Rev. Sci. Instrum. **68**, 3477 (1997).
[14] A. Sanov and W. C. Lineberger, PhysChemComm **5**(25), 165 (2002); A. Sanov and W. C. Lineberger, Phys. Chem. Chem. Phys. **6**, 2018 (2004).
[15] A. J. R. Heck and D. W. Chandler, Annu. Rev. Phys. Chem. **46**, 335 (1995).
[16] V. Dribinski, A. Ossadtchi, V. A. Mandelshtam, and H. Reisler, Rev. Sci. Instrum. **73**, 2634 (2002).
[17] G. A. Garcia, L. Nahon, and I. Powis, Rev. Sci. Instrum. **75**, 4989 (2004).
[18] W. Li, S. D. Chambreau, S. A. Lahankar, and A. G. Suits, Rev. Sci. Instrum. **76**, 063106 (2005).
[19] F. Breyer, P. Frey, and H. Hotop, Z. Phys. A: Hadrons Nucl. **286**, 133 (1978).
[20] M. J. Frisch, G. W. Trucks, H. B. Schlegel *et al.*, GAUSSIAN 03, Revision C.02, Gaussian, Inc, Wallingford CT, 2004.
[21] A. D. Becke, J. Chem. Phys. **98**, 5648 (1993); C. T. Lee, W. T. Yang, and R. G. Parr, Phys. Rev. B **37**, 785 (1988).
[22] A. D. McLean and G. S. Chandler, J. Chem. Phys. **72**, 5639 (1980); R. Krishnan, J. S. Binkley, R. Seeger, and J. A. Pople, *ibid.* **72**, 650 (1980).
[23] J. A. Pople, M. Head-Gordon, and K. Raghavachari, J. Chem. Phys. **87**, 5968 (1987).
[24] T. H. Dunning, Jr., J. Chem. Phys. **90**, 1007 (1989).
[25] K. M. Ervin, T. M. Ramond, G. E. Davico, R. L. Schwartz, S. M. Casey, and W. C. Lineberger, J. Phys. Chem. A **105**, 10822 (2001).
[26] K. M. Ervin, PESCAL, University of Nevada, Reno, 2008.
[27] F. Duschinsky, Acta Physicochim. URSS **7**, 551 (1937).
[28] T. E. Sharp and H. M. Rosenstock, J. Chem. Phys. **41**, 3453 (1964).
[29] P. Chen, in *Unimolecular and Bimolecular Reaction Dynamics*, edited by C.-Y. Ng, T. Baer, and I. Powis (Wiley, Chichester, 1994), p. 371.
[30] D. Gorse, D. Cavagnat, M. Pesquer, and C. Lapouge, J. Phys. Chem. **97**, 4262 (1993).
[31] L. H. Spangler, Annu. Rev. Phys. Chem. **48**, 481 (1997).
[32] A. L. L. East and L. Radom, J. Chem. Phys. **106**, 6655 (1997).
[33] K. C. Ingham and S. J. Strickler, J. Chem. Phys. **53**, 4313 (1970).
[34] L. H. Spangler and D. W. Pratt, J. Chem. Phys. **84**, 4789 (1986).
[35] C. N. Yang, Phys. Rev. **74**, 764 (1968).
[36] J. Cooper and R. N. Zare, J. Chem. Phys. **48**, 942 (1968).
[37] E. P. Wigner, Phys. Rev. **73**, 1002 (1948).
[38] P. C. Engelking, Phys. Rev. A **26**, 740 (1982); J. R. Smith, J. B. Kim, and W. C. Lineberger, *ibid.* **55**, 2036 (1997).
[39] J. L. Hall and M. W. Siegel, J. Chem. Phys. **48**, 943 (1968).
[40] C. H. Greene, Phys. Rev. Lett. **44**, 869 (1980); C. Pan, A. F. Starace, and C. H. Greene, J. Phys. B **27**, L137 (1994).
[41] K. M. Ervin, J. Ho, and W. C. Lineberger, J. Phys. Chem. **92**, 5405 (1988).
[42] C. T. Wickham-Jones, K. M. Ervin, G. B. Ellison, and W. C. Lineberger, J. Chem. Phys. **91**, 2762 (1989).
[43] K. M. Ervin and W. C. Lineberger, in *Advances in Gas Phase Ion Chemistry*, edited by N. G. Adams and L. M. Babcock (JAI, Greenwich, CT, 1992), p. 121.
[44] K. J. Reed, A. H. Zimmerman, H. C. Andersen, and J. I. Brauman, J. Chem. Phys. **64**, 1368 (1976).
[45] W. B. Clodius, R. M. Stehman, and S. B. Woo, Phys. Rev. A **28**, 760 (1983); R. M. Stehman and S. B. Woo, *ibid.* **23**, 2866 (1981).
[46] H. W. W. Massey, *Negative Ions* (Cambridge University Press, Cambridge, 1976).
[47] K. M. Ervin, J. Ho, and W. C. Lineberger, J. Chem. Phys. **91**, 5974 (1989).
[48] E. Surber and A. Sanov, J. Chem. Phys. **116**, 5921 (2002).
[49] See EPAPS Document No. E-JCPSA6-130-031906 for calculated geometries of $CH_3NO_2^-$ and CH_3NO_2, as well as parameters and more details on the Franck–Condon simulations described in the text. For more information on EPAPS, see http://www.aip.org/pubservs/epaps.html.